AIAA JOURNAL
Vol. 59, No. 6, June 2021

Smart Solar Array Consisting of Shape-Memory Releasing Mechanisms and Deployable Hinges

Xin Lan,* Liwu Liu,† Chengtong Pan,‡ Fengfeng Li,§ Zhengxian Liu,¶ Guanghua Hou,** Jian Sun,††
Wenxu Dai,‡‡ Linlin Wang,§§ Honghao Yue,¶¶ Yanju Liu,*** and Jinsong Leng†††
Harbin Institute of Technology, 150001 Harbin, People's Republic of China
and
Xiaoqing Zhong‡‡‡ and Yong Tang§§§
Chinese Academy of Space Technology, 100094 Beijing, People's Republic of China

https://doi.org/10.2514/1.J059281

Based on our previous successful material-level verification of a shape-memory polymer composite (SMPC) on the SJ-17 geostationary satellite on a geostationary orbit since November 2016, a structure-level smart solar array was developed in this study to further verify its overall performance on the SJ-18 geostationary satellite. The two-panel smart solar array based on shape-memory materials was designed and experimentally evaluated. The smart solar array consisted of two deployable solar panels, which were locked by one shape-memory alloy and two SMPC releasing mechanisms, and could be released by low shocking through electrical heating. The smart solar array was actuated and deployed using two groups of SMPC hinges. A series of tests was conducted to evaluate the main performance of the smart solar array. The tests included structural dynamics (folded state: sinusoidal sweep vibration, shocking, acceleration, and noise; and deployed state: mode, sinusoidal sweep vibration, and flexibility), thermal design, locking and releasing, and deployment. This smart solar array satisfied the design requirements, including the fundamental natural frequency in a folded state at 80 Hz, maximum the locking force at 2000 N. Based on the structure-level systematical evaluation, the SMPC shows prospect to be used in next-generation superlarge deployment structures.

I. Introduction

SPACE deployable structures (e.g., solar arrays, trusses, and antennas) based on smart materials have been developed in recent years [1]. Origami-inspired materials and structures may be applied for space deployable solar arrays or trusses through stacked Miura origami with flexible crease lines [2]. A tip-extending soft robot can increase its length for deployment and reconfiguration of new-generation space deployable antennas [3].

As traditional structure materials, fiber-reinforced polymer composites have been widely used in aerospace structures. In the design of these traditional composite structures, the large geometrical deformation should be forbidden to avoid structure instability, and hence the maximum strain of traditional composites is usually selected to be lower than 0.5% [4]. In recent years, research on flexible composites for space deployable structures has been active [5–11]. To realize automatic deployment without external force actuation, the high-strain composite structures with internal stowed strain energy have been proposed. The maximum reversible strain of thin-wall high-strain composite structures could be as high as 1.5–2%, which almost approaches the strain limit of composite materials [5–7]. In this way, the thin-wall high-strain composite structures could produce large macroscopic deflection and angular deformation through a specific direction stiffness coupling design as well as reduce thickness [9,10]. For instance, with the maximum strain of 1.5% of a thin-walled high-strain composite (thickness of 0.2 mm), its minimum radius of curvature can reach 6.66 mm. This thin-walled high-strain composite structure can be used for space autoexpanding structures. On the basis of these design ideas, the rollout solar array (ROSA) was developed by NASA and the U.S. Air Force Laboratory, and its deployment on the International Space Station was successfully verified in 2016 [12,13]. The ROSA deployable structure [12,13] adopts a thin-wall high-strain composite material (maximum strain is supposed to be approximately 1.5%), and the maximum thickness of the structure is approximately 0.2 mm under the general design requirement of the unfolding/folding ratio.

Shape-memory polymers (SMPs) are variable-stiffness materials [14]. When the temperature of a SMP is much lower than its glass transition temperature T_g, its stiffness and creep effect are at the same level of traditional plastics [15]; When it is above the T_g, the SMP is soft and the strain limit could be as high as 100%. In this way, fiber-reinforced SMP composites (SMPCs) show compressive or bending large-deformation characteristics in a soft SMP matrix above T_g [16–23]. Given the microbuckling of fibers in the soft SMP matrix, the maximum reversible compressive strain of SMPCs can reach 8–10% [19,22]. Therefore, with the same form of structural design as the thin-wall high-strain composite (thickness 0.2 mm), the maximum thickness of SMPC structures can reach as high as 0.6 mm with the same curvature [19,22], and therefore they could significantly improve the stiffness and fundamental frequency of the foldable

Received 26 November 2019; revision received 7 August 2020; accepted for publication 22 October 2020; published online 23 April 2021.

*Associated Professor, Center for Composite Materials and Structures; lanxin@hit.edu.cn.
†Professor, Department of Astronautical Science and Mechanics; liuliwu_006@163.com.
‡Ph.D. Student, Center for Composite Materials and Structures; pct1136144344@163.com.
§Postdoctor, Department of Astronautical Science and Mechanics; eastlifelifengfeng@126.com.
¶Ph.D. Student, Department of Astronautical Science and Mechanics; liuzhengxian_hit@qq.com.
**Ph.D. Student, Department of Astronautical Science and Mechanics; houbaohua@126.com.
††Associated Professor, Center for Composite Materials and Structures; sunjianhit@163.com.
‡‡Engineer, Department of Astronautical Science and Mechanics; 1241549917@qq.com.
§§Ph.D. Student, Center for Composite Materials and Structures; wangll_hit@163.com.
¶¶Professor, School of Mechatronic Engineering; yuehonghao@hit.edu.cn.
***Professor, Department of Astronautical Science and Mechanics; yj_liu@hit.edu.cn.
†††Professor, Center for Composite Materials and Structures; lengjs@hit.edu.cn (Corresponding Author).
‡‡‡Senior Engineer, Institute of Telecommunication Satellite, P.O. Box 5142, No. 104 Youyi Street, Haidian District; hitzxq@126.com.
§§§Senior Engineer, Institute of Telecommunication Satellite, P.O. Box 5142, No. 104 Youyi Street, Haidian District; txwx_tangyong@163.com.

space structure in the deployed state. However, under the premise that the fundamental frequency of the deployed state is constant, the ultimate expansion area is much larger in the deployable structure based on the SMPC than in the thin-wall high-strain composites [21–23]. In summary, the SMPC and its space deployable structure demonstrate the following advantages:

1) Given microbuckling, the SMPC structure can be bent and folded to obtain a large expansion/contraction rate and maintain a high fundamental frequency [22,23], which can be applied to space deployable hinges, trusses, and antennas.

2) SMPC structures have dual functions, namely, structural loading and active deformation actuation [24,25]; these functions may be used for the locking and releasing mechanisms.

The triggering process of the SMPC is determined by the T_g of the SMP material. It requires the damping to be large, the releasing duration to be long (10–30 s), and the shocking to be low (less than $1g$). Thus, it may overcome the reliability risk of shocking-sensitive components in satellites caused by the huge transient shocking in the releasing process of traditional electroexplosive devices (releasing duration: 0.02–0.05 s, and transient shocking: $3 \times 10^2 - 3 \times 10^5 g$) [26,27].

Several experiments in low Earth orbit have been conducted to evaluate the shape-memory effect (SME) of SMPs or SMPCs, including the TEMBO® elastic memory composite hinge and gravity gradient boom [16,17], as well as SMP foam [28,29]. To expand their applications to a broad space environment, Li et al. developed and conducted an evaluation of the SME of a deployable solar array substrate fabricated using epoxy-based SMPC laminates in a geostationary orbit (36,000 km) in November 2016 [30]. Its shape recovery ratio was 100%, and the surface was observed through a hand–eye camera outside the satellite in December 2018.

The explosion shock generated by the traditional electroexplosive device during unlocking is a serious mechanical environment experienced by nearly all spacecraft [31–33]. Shape-memory-alloy-based releasing devices [34,35] show the following advantages over the traditional electroexplosive device: these devices can reduce shocking during separation and releasing, no harmful gases or debris are generated when gunpowder is burned or exploded, and they do not pollute the surrounding environment. SMAs can be used multiple times; thus, they are convenient for test verification, and the reliability of the release devices is easy to ensure [36]. The components of a unit mass can output additional power with SMAs. The miniaturization and weight reduction of the connection and separation devices are realized, and the launch cost of the spacecraft is reduced [37].

Considering the deformation behavior of the SMA and SMPC, the thermal–mechanical constitutive relations involve three key parameters, namely, stress, strain, and temperature. The SMA releasing mechanisms, SMPC releasing mechanisms, and SMPC deployable mechanisms are expected to be applied to the next generation of superlarge deployable structures, such as flexible solar arrays, hoods, and solar sails. These mechanisms may play important roles in the innovation and development of aerospace technology.

On the basis of Li et al.'s previous evaluation of SMPCs in mission SJ-17 in a geostationary orbit (36,000 km) [30], a space deployable smart solar array without a traditional electroexplosive device or mechanical hinge driving structure was proposed in the present study. The SMPC was used to fabricate releasing and deployment devices, and the SMA was used to fabricate the releasing devices. In accordance with China's aerospace standards, the design and performance evaluations of a smart solar array based on shape-memory materials were systematically conducted.

II. Structural Design and Analysis of the Smart Solar Array

A. Main Design of the Smart Solar Array

The smart solar array consists of two solar panels. It is locked by one SMA- and two SMPC-based releasing mechanisms. Then, this device is released by electrical heating the two types of releasing devices and finally deployed using four SMPC-based hinges (two 90 deg and two 180 deg hinges) through electrical heating. When it is deployed, the self-locking mechanism is triggered to maintain the deployment configuration and structural stiffness. The smart solar array is composed of the following six parts (Fig. 1 and Table 1): structural frame (I), solar panels (two pieces; II), SMA releasing mechanism (III), SMPC releasing mechanisms (two groups; IV), SMPC hinge actuation mechanisms (V), hold-down mechanism (VI), and self-locking mechanism (VII). Considering the unfolding process, two SMPC hinges (V-1; predeformation angle of 90 deg and total power of 100 W) connect the base (satellite deck) with the solar panel (II-1). Another two SMPC hinges (V-2; predeformation angle of 180 deg and total power of 100 W) connect solar panel II-1 with solar panel II-2. The outermost size of this solar array structure is $628 \times 650 \times 185$ mm in folded shape and $381 \times 650 \times 1379$ mm during and after deployment. During the deployment process, the length decreases from 628 to 381 mm, whereas the height increases from 185 to 1379 mm. The structural installation position was reserved on the side deck of the satellite and punched holes for connection of the solar array. All SMPC hinges have a shape recovery rate of approximately 98–100%. The overall weight of the smart solar array is 11.8 kg.

B. Design of the Solar Panel and Mainframe

Figure 2 illustrates the structural design (Fig. 2a) and physical object (Fig. 2b) of solar panel II-1. The solar array consists of two deployable solar panels. The solar panels are aluminum honeycomb sandwich panel structures, which effectively reduce the weight under

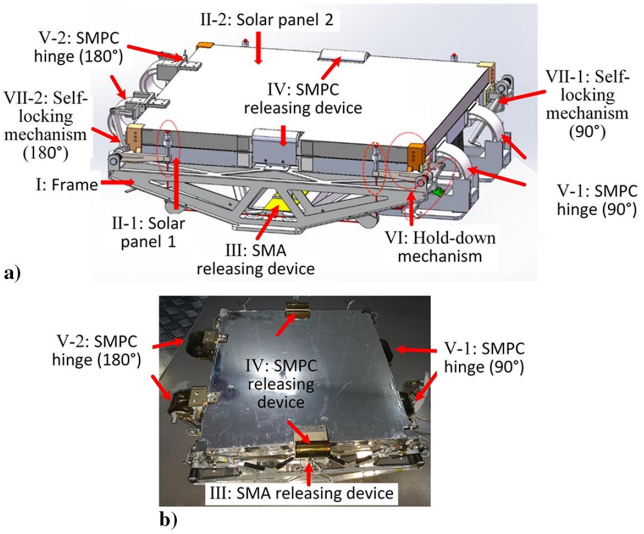

Fig. 1 Smart solar arrays: a) structural design, and b) physical objects.

Table 1 Main parameters of the smart solar arrays

Items	Value
Mass	11.8 kg
Structure	Two solar panels, deployment in two steps
Folded outermost size	(628 ± 5) mm × (648 ± 1) mm × (185 ± 5) mm
Deployment outermost size	(381 ± 2) mm × (632 ± 2) mm × (1379 ± 5) mm
First frequency in a folded configuration	79.70 Hz
Deployment duration	Total deployment time of 10–12 min
Heating power	90 deg hinge: 25 W (250 Ω); a 180 deg hinge: 25 W (250 Ω)
	SMA releasing mechanism: 18 W (7.8 Ω)
	SMPC releasing mechanism: 29 W (250 Ω)
Transition temperature	90 deg hinge: 150°C; 180 deg hinge: 150°C
	SMA releasing mechanism: 95°C
	SMPC releasing mechanism: 210°C
Shape recovery ratio	98–100%
Design life	2 years

the premise of ensuring structural strength. In Fig. 2, the aluminum embedded parts on the four sides around the solar panel are designed to realize the installation of the locking mechanism and hinge joint. The four corners are also punched with holes for easy lifting. The chamfer has two rectangular embedded parts with pinholes inside for pressing. The dimensions of the aluminum honeycomb sandwich panel are $500 \times 500 \times 19$ mm, with a resistance temperature of -100 to $+120$°C and a weight of 2.5 kg (10 kg/m^2 and thickness of 19 mm).

Regarding the structure design of a space flight hardware, some strict constraint conditions should be satisfied. For the structure design of the smart solar arrays, the primary constraint conditions include the total mass of ≤ 15 kg, the area of a single solar panel of 0.5×0.5 m (total two solar panels), a fundamental frequency of ≥ 80 Hz, and enough strength. One cycle of structure optimizing design usually undergoes the following steps (as shown in Fig. 3): 1) structure design, 2) simulation analysis by the finite element method (FEM), 3) vibration experiments, 4) FEM model modification, and 5) optimized structure design. For the FEM analysis, the solar panel was modeled using shell elements, and the mainframe was modeled with solid elements. In particular, the connecting stiffness of the FEM was difficult to be specified, which may mainly affect the dynamics performance. To artificially adjust the connecting stiffness of adjacent components at some essential positions, the beam elements were used in the FEM model. In the initial stage of FEM analysis of the smart solar array in a folded state, the connecting stiffness was specified to a certain value based on experiences. After the sinusoidal sweep vibration test, the first and second natural frequencies, strains, and stresses at some important locations could be obtained. On the basis of these experimental results, the special beam elements were artificially adjusted to make the FEM natural frequencies approach the experimental results. Meanwhile, as determinant conditions, the FEM stresses should also approach the according experimental results. Through the aforementioned model adjustment based on experimental results, the adjusted FEM model was considered as a "real numerical model" of the smart solar arrays. Base on this adjusted FEM model, the structural optimization can be conducted. That is, on the premise that the strength satisfied the related demands and the fundamental frequency was higher than 80 Hz, the mass should be reduced as much as possible. After that, the structure design and corresponding FEM model were modified in the second turn of the optimization stage. Then, the vibration performance was tested again. In this way, after more than three primary turns of structure optimization, the current form of structure design was obtained, where the lowest value of experimentally fundamental frequency was 79.70 Hz in the X direction and the mass was reduced to 11.8 kg. Note that, due to the complex optimization procedures, another paper will be published to specifically study the mechanical optimization design.

The mainframe is composed of a double inverted trapezoidal fixing bracket, double X-shaped fixing frames, struts, and hinge connecting bases. The inverted trapezoidal bracket is directly connected to the satellite deck. To increase the rigidity of the entire structure, the X-shaped bracket is connected to the base of the 90 deg hinge using the struts. Figures 4a and 4b depict the design and physical objects of the bottom view of the frame structure, respectively. To facilitate the understanding of the structural design, Fig. 4c exhibits the design of the front view of the solar array excluding the honeycomb sandwich panel. The solar array has four metallic bases connected to the satellite deck: each of which has four bolt holes at the four corners, and the center distance of the bolt holes is 100 mm. The frame material is made of aerospace-grade 7075 aluminum. The processing technology and precision control strictly follow the related aerospace standards. The surfaces with relatively moving contacts are treated with molybdenum to prevent cold welding between the friction components. All processing and manufacturing departments are qualified for China's aerospace.

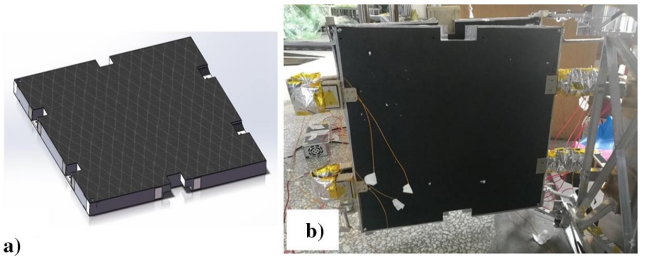

Fig. 2 Structural design and physical objects of the smart solar array: a) structural design, and b) physical objects.

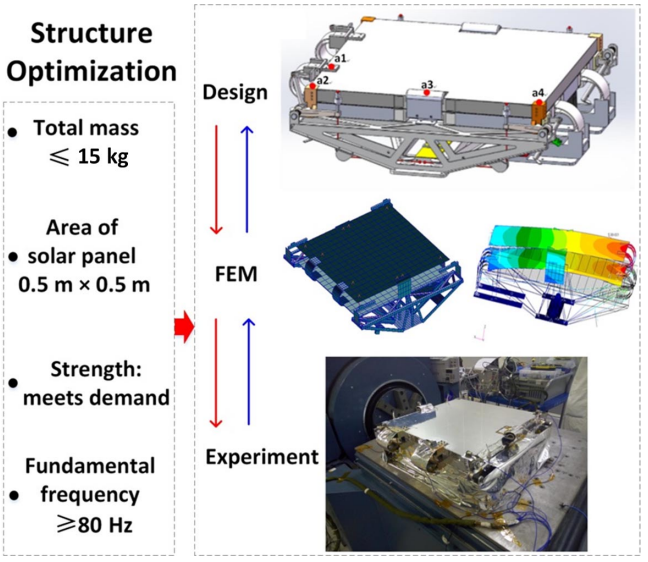

Fig. 3 Illustration of structure optimization of the smart solar array.

C. SMA Releasing and Pretensioning Mechanisms

The releasing mechanism is mainly based on an SMA expander, as demonstrated in Fig. 5a, mounted at the center of the bottom of the support plate (Fig. 5b). The SMA expander is composed of an SMA rod, a slotted titanium rod, a limit hollow cylinder, a cushion, and a support plate. Figure 5 shows its SMA expander physical objects (Fig. 5a1), design of SMA expander in locked state (Fig. 5a2),

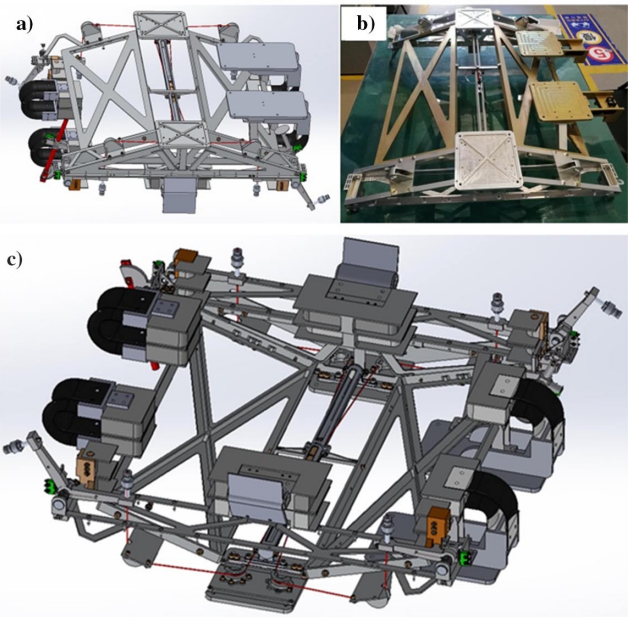

Fig. 4 Design and physical objects of frame structure of smart solar array: the design a) and physical objects b) of the bottom view of the frame structure; the design of the front view of the solar array c) excluding the honeycomb sandwich panel.

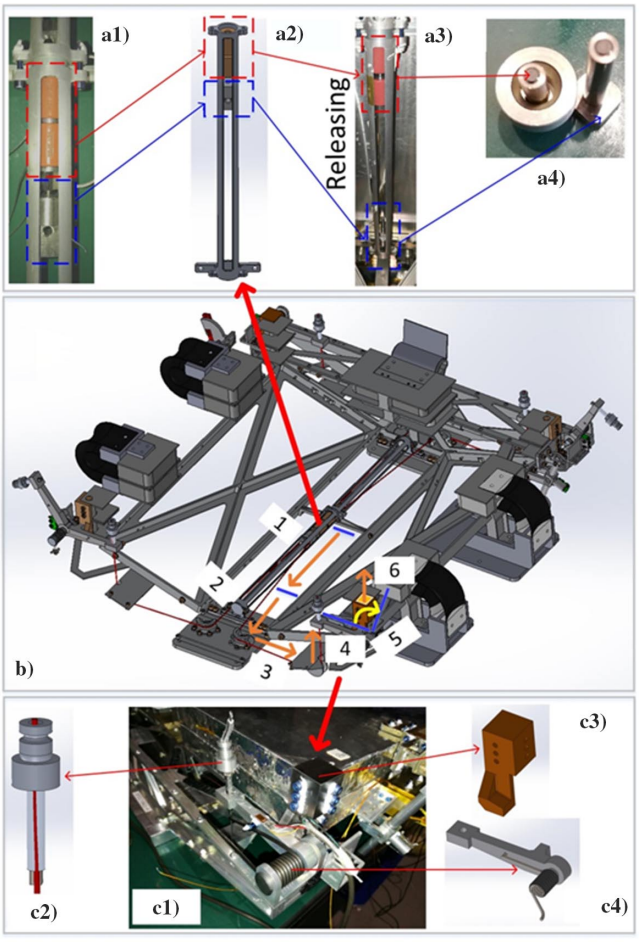

Fig. 5 SMA-based releasing and pretensioning mechanism: a1)–a4) SMA expander physical objects; b) SMA expander mounted at center of bottom of support plate and releasing processes 1–6; c1)–c4) pretensioning and pressing mechanism.

released SMA expander (Fig. 5a3), and broken titanium rod (Fig. 5a4).

The pretensioning mechanism (Fig. 5c1) includes a pretensioning head (Fig. 5c2), a spherical pin (Fig. 5c3), a pressing rod. and a torsion spring (Fig. 5c4). The shaft is directly mounted on the inverted trapezoidal fixing bracket, and the torsion spring is arranged on this shaft. The spherical pins in the holes are fixed at the four corners of the solar panel. The Kevlar string provides a pulling force at one end of the pressing rod; thus, the pressing rod rotates around the shaft, and the inclined surface of the pressing rod is pressed against the inclined surface of the solar panel to provide a vertical downward and horizontal pressing force. Simultaneously, the coordination of the spherical pinholes at the four corners constrains the freedom of the remaining directions of the solar panel to achieve locking. In Fig. 5c2, the pretensioning head is composed of a pretensioning ball head, a pretensioning cylinder, a pretensioning bolt, a nut, a Kevlar fiber rope, and a steering device. A section of the Kevlar string is connected to the SMA expander through two pretensioning mechanisms using two steering devices. The tension on the Kevlar string is changed by adjusting the pretensioning thread to achieve the designed pretensioning force.

The SMA expander pulls the Kevlar string before and during the launch of the satellite. Thus, the pressure bars firmly press the four bottoms of the solar panel to ensure the reliable application and retention of the locking force. When the solar array is positioned on the space orbit with the satellite, the SMA expander is electrically heated, and the SMA expander deforms to break the titanium rod (Fig. 5b; processes 3 and 4). The titanium rod slides along the limited hollow cylinder to the two ends and hits the cushion (Fig. 5b, process 1); the Kevlar string is released, and the pretensioning rod returns to the initial state under the action of the torsion spring to release the hard connection (Fig. 5b; processes 1–5); and thus, the smart solar array can be freely deployed (Fig. 5b; process 6).

D. SMPC Releasing Mechanisms

In addition to the SMA releasing mechanism, the releasing mechanism system of the solar array developed in this study contains an SMPC releasing mechanism (Fig. 1; item IV), wherein double pieces of SMPC laminates are bent and pressed on both sides of the solar panel (Fig. 1; item II-2). The SMPC releasing mechanism must be electrically heated after unlocking the SMA releasing mechanism.

The SMPC releasing mechanism primarily consisted of a SMPC locking/releasing laminate, which was a carbon-fiber-reinforced SMP. The matrix of the composite was a cyanate-based SMP with $T_g = 210$°C, which was synthesized by Xie et al. [38]. The reinforcement of the composite was two layers of commercial carbon-fiber twill fabrics (Toray T300-3 K), which was layered at $+45/-45$ deg along the length direction of the SMPC laminate. The SMPC locking/releasing laminate was made by vacuum-assisted resin transfer molding [39]. The thickness of the SMPC locking/releasing laminate was 1.6 mm with the carbon fiber reinforcement of 25% in volume fraction. Considering the systematical material parameters (e.g., dynamic mechanics versus temperature, elastic modulus and strength of elongation, bending modulus and strength, shape recovery ratio, relaxation, and creep properties), the composite structure was designed using the theory of bending large-deformation based on previous studies by Lan et al. [19,22]. Especially due to fiber microbuckling in the relatively soft SMP matrix, the SMPC locking/releasing laminate could obtain a maximum 10% reversible compressive strain at macroscale. In this way, in order to obtain a high unfolding/folding ratio, the maximum compressive strain on the inner surface was designed as about 7.58% considering the safety margin, and therefore the minimum curvature radius could be as small as 20 mm (material thickness of 1.6 mm).

For the SMPC releasing mechanism, one electrical heating chip was attached on the outer side of the SMPC locking/releasing laminate to realize the electrical heating for the SMPC. A heat insulation multilayer component was used to ensure the temperature of the SMPC releasing mechanism between −120 and +50°C on orbit. Therefore, the outer surface of the SMPC releasing mechanism was covered with five units of heat insulation multilayer components, and the outermost layer was a single-sided aluminum-plated antistatic F46 film.

In Fig. 6, the curved laminate in the locked state gradually returns to the straight released state, and then the two solar panels are in the releasable state. Then, the SMPC hinges are electrically heated, and the smart solar array is actuated for deployment. Note that, because of the complexity of the research and development of SMPC releasing mechanism, another paper will be published to specifically discuss its whole process of design, including SMPC material properties, structural mechanics theory, design, and deployment performance evaluations.

E. SMPC Hinges

The actuation mechanisms include four SMPC hinges, namely, two 90 deg hinges (Fig. 7a) and two 180 deg hinges (Fig. 7b). The related design, analysis, characterization, and ground-based evaluation of the

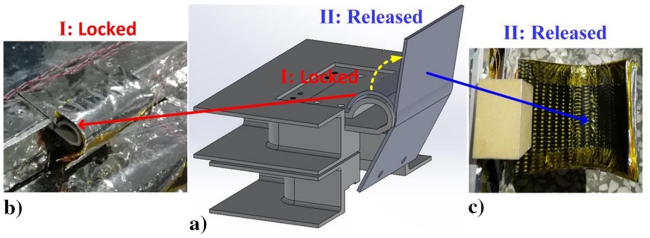

Fig. 6 SMPC-based releasing mechanism: a) illustration from locked state to released state, b) locked state of physical objects, and c) released state of physical objects.

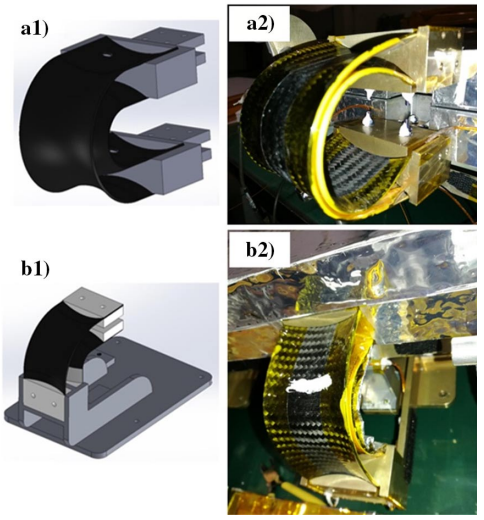

Fig. 7 SMPC hinge: a1–a2) 90 deg hinge, and b1–b2) 180 deg hinge.

SMPC hinges have been published in previous literature by Liu et al. [40]. The 90 deg hinges connect the base with solar panel-1; the 180 deg hinges connect solar panel 1 and solar panel 2. The main components of each hinge are two pieces of curved SMPC laminates, and the hinge was made into the shapes of two tape springs located in the opposite directions. During the bending deformation, as shown in Fig. 7a1, the inner SMPC laminate is bent in the equal sense, and the outer one is in the opposite sense. Each curved SMPC laminate was attached with electrically resistive films for joule heat excitation to trigger the shape recovery. The hinges act as a load-carrying structure and a deployment actuation mechanism. The SMPC is an epoxy-based carbon-fiber-reinforced composite at a glass transition temperature of 150°C. The smart solar array is folded before launching the satellite. When the satellite reaches the predetermined orbit and the deployment command is released, the SMPC hinges are electrically heated using a satellite power supply system. When the temperature reaches the glass transition temperature, the bent 90 or 180 deg SMPC hinge returns to the original straight shape, and the smart solar array realizes the deployment.

F. Self-Locking Mechanism for Solar Panels

When the SMPC hinges have driven a solar panel, the self-locking mechanism is also required to lock its deployed state rigidly. The 90 deg locking mechanism connects the base with solar panel 1; the 180 deg locking mechanism connects solar panel 1 and solar panel 2. In Fig. 8, the self-locking mechanism is composed of a positioning pin, a movable rod, and a positioning pin hole. With the unfolding of the solar panel, the movable rod rotates around the shaft simultaneously, and the positioning pin gradually slides along the movable rod. When the SMPC hinges deploy into the desired angle, the dowel will automatically inset into the pinhole to lock the deployed solar, which is also a structural component for the deployed solar panel. At the same time, the microswitch is trigged when its reed contacts the baffle at the end of the movable rod. The trigging signal of the microswitch will immediately transfer from the SJ-18 satellite on Earth synchronous orbit to the ground, which could indicate that the solar panel has been deployed into the desired configuration.

G. Deployment Procedure for the Smart Solar Array

The main deployment procedure of the smart solar array based on the SMPC hinge is as follows. At the unfolded state (Fig. 9a), the smart solar array is locked through the SMA releasing/pretensioning mechanism, and the pretensioning force in the Kevlar string is adjusted using a pretightening thread, which provides a reasonable locking stiffness, and therefore constrains the smart solar array. When the SMA expansion device is electrically heated, the expansion deformation rapidly breaks the titanium rod of the groove, and

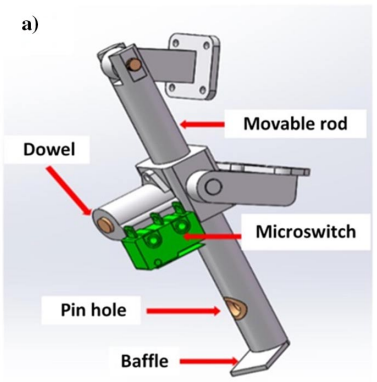

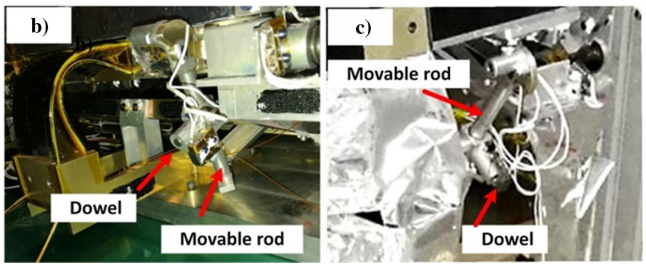

Fig. 8 Design and physical objects of the self-locking mechanism of the solar panel: a) structural design, b) physical objects in folded state, and c) physical objects in deployed state.

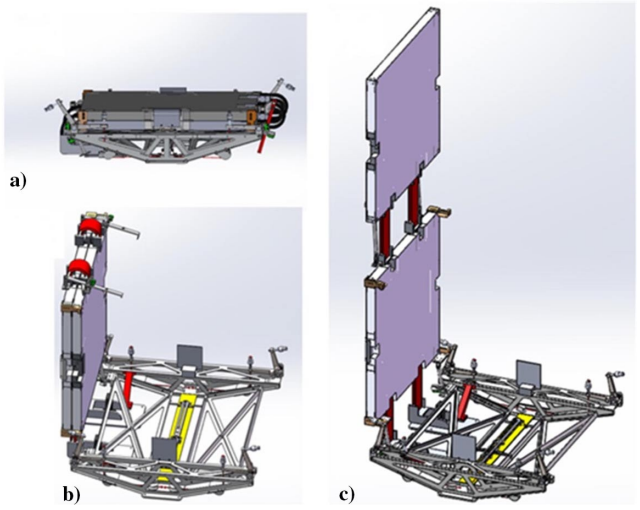

Fig. 9 Deployment procedure of the smart solar array: a) folded state, b) intermediate state, and c) deployment state.

the Kevlar string pulls the titanium rod along the limited hollow cylinder to the two ends and hits the cushion. Then, the pressure rod rotates around the shaft under the action of the torsion spring and releases four pressure feet on the solar panel. Then, the SMPC releasing mechanism is gradually unfolded through electrical heating, and the constraint of the smart solar array is completely removed. The 90 deg SMPC hinge is then electrically heated to return to its original straight state, and the solar array expands to the state, as presented in Fig. 9b. Moreover, to lock solar panel 1 in the deployment state using the 90 deg locking mechanism, the movable rod rotates around the shaft while the smart solar array is in the intermediate state, and the positioning pin slides along the movable rod to the positioning hole. Subsequently, the 180 deg SMPC hinge is electrically heated, and the smart solar array is deployed. In a procedure similar to the 90 deg locking mechanism, the 180 deg locking mechanism locks solar panel 2, and the final state is illustrated in Fig. 9c.

III. Experimental Evaluation of the Main Performance of the Smart Solar Array

A. Structural Dynamics Performance

The structural dynamics tests mainly determine whether the structure is damaged under the ground simulated mechanical conditions of a folded state and whether it ensures its structural stiffness in a deployed state. Structural mechanical property tests include sinusoidal sweep vibration, shock, acceleration, and noise in a folded state and mode; sinusoidal sweep; and stiffness in a deployed state.

1. *Sinusoidal Sweep Vibration Test (Folded State)*

One sinusoidal sweep vibration test for the folded smart solar array has three steps, as follows: 0.2g characteristic sweep, acceptance level of sweep evaluation, and the repeated 0.2g characteristic sweep. In each step, the sweeping vibration tests were conducted in three directions, as depicted in Fig. 10, where the X, Y, and Z directions are defined. Four unidirectional accelerometers (point 1–point 4) were used to test the acceleration response. As the SMPC hinges and SMPC releasing mechanisms were sensitive components, point 1 and point 2 were located on the SMPC hinge and SMPC releasing mechanism, respectively. Furthermore, because the corners of the solar panel were sensitive locations for vibration testing, point 3 and point 4 were placed on the two adjacent corners of the solar panel. The test direction of each sensor was changed to the direction of resonance force when alternating vibrating direction. Note that three axes' accelerometers were not used in the testing, and the cross-coupling vibration responses were not considered. The 0.2g characteristic sweep was conducted at the frequency range of 5–1000 Hz, and the acceleration amplitude was 0.2g with a sweep speed of 4 octave per minute (oct/min). For the acceptance sweep evaluation, the vibration magnitudes in the X direction are 5–20 Hz, 5 mm (half-amplitude, zero-peek); 20–83 Hz, 8g (4 oct/min); and 83–100 Hz, 7g (4 oct/min). In the Y and Z directions, the vibration magnitudes are 5–20 Hz, 5 mm; and 20–100 Hz, 8g (4 oct/min). Then, the repeated 0.2g characteristic sweep was performed to evaluate the dynamics stability. Video recording was performed during the experiment to observe any damage. The structural inspection was performed after each experiment.

The dynamics responses of a typical measuring point (point 1 highlighted in Fig. 10) in three directions are summarized in Table 2 and Fig. 11. From the 0.2g sinusoidal characteristic sweeping results, the first natural frequency of the smart solar array is constant at approximately 87 Hz in the X and Z directions. In Y direction after an 8g sinusoidal sweep vibration, the fundamental frequency dropped from 121.00 to 112.7 Hz, which indicated the variation of structural status. Hence, the structure of the smart solar array was carefully checked, and a screw was found to be loose because of the inadequate pretightening torsion during assembling. Therefore, a new screw was used, and the 1.2-time rated pretightening torsion was applied on it. Furthermore, the silicon rubber was overlaid on the surface of the new screw; and after solidification, it could prevent loosening of the screw.

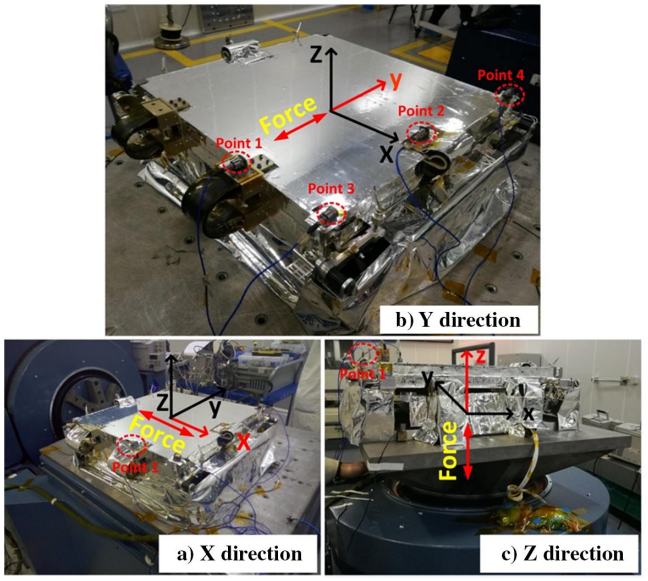

Fig. 10 Sinusoidal sweep vibration experiments of the smart solar array (folded state).

Table 2 Sine sweep test results of the smart solar array (folded state, point 1)

Direction	Condition	Frequency, Hz	Amplitude, g
X	0.2g sweep	87.96	1.69
	8g acceptance evaluation	79.70	34.67
	Repeated 0.2g sweep	86.93	1.67
Y	0.2g sweep	121.00	6.53
	8g acceptance evaluation	99.34	38.63
	Repeated 0.2g sweep	112.7	6.30
Z	0.2g sweep	87.96	1.84
	8g acceptance evaluation	82.41	72.44
	Repeated 0.2g sweep	87.96	2.20

From the 8g acceptance vibration evaluation results, the amplitudes of the acceleration resonance responses are 34.67g (79.70 Hz) in the X direction, 38.63g (99.34 Hz) in the Y direction, and 72.44g (82.41 Hz) in the Z direction. Note that the maximum value of the peak of the acceleration response in the Z direction was 72.44g, which exceeded the normal maximum value of 60g. Accordingly, in order to ensure the structural safety, the structure of the smart solar array after vibration tests was carefully checked and confirmed to be free from damage. In addition, according to the general experience, the first natural frequency of the structures in a folded state should be no less than 80 Hz. Accordingly, the lowest value of the first natural frequency was 79.70 Hz in the X direction, which was considered to satisfy the aforementioned demand. In summary, through the sinusoidal sweep vibration tests of the folded smart solar array in the X, Y, and Z directions, the first natural frequencies and the peaks of acceleration response satisfied the demands of the related structural dynamics performance for space flight. Upon passing the performance evaluation in ground simulated vibration conditions, the structure of the smart solar array exhibited high enough stiffness and strength to withstand the possible vibration conditions during the launching process. Furthermore, the resonance amplitudes were also in the range of design prediction that could ensure the structure safety, even when suffering the resonance conditions.

2. *Shocking Test (Folded State)*

To ensure the safety of the smart solar array in the launching process aboard the satellite, the shocking test under the ground simulated mechanical conditions of a folded state needs to be evaluated. The shocking test was conducted in three directions, as demonstrated in Fig. 12, to verify the structural reliability of the smart solar array under a possible shocking condition. The locations of the accelerometers of the shocking test were the same as those of the sinusoidal sweep vibration experiments in Fig. 10a. As shown in Fig. 13a, the shocking spectrum is specified as 100–1500 Hz, +6dB/oct; and 1500–4000 Hz, 1600g, where the upper and lower limits of the shock control curves are also shown. The tests were repeated at least three times in each direction. As shown in Fig. 13b, the shocking response duration is approximately 10 μs, and the maximum amplitude of the transient response is nearly 1000g. The appearance of the solar array structure after all the shocking tests was normal, and therefore the smart solar array could withstand the designed shocking conditions to ensure the safety to ensure the safety in case of suffering some incident shocking (e.g., launching process, transportation process).

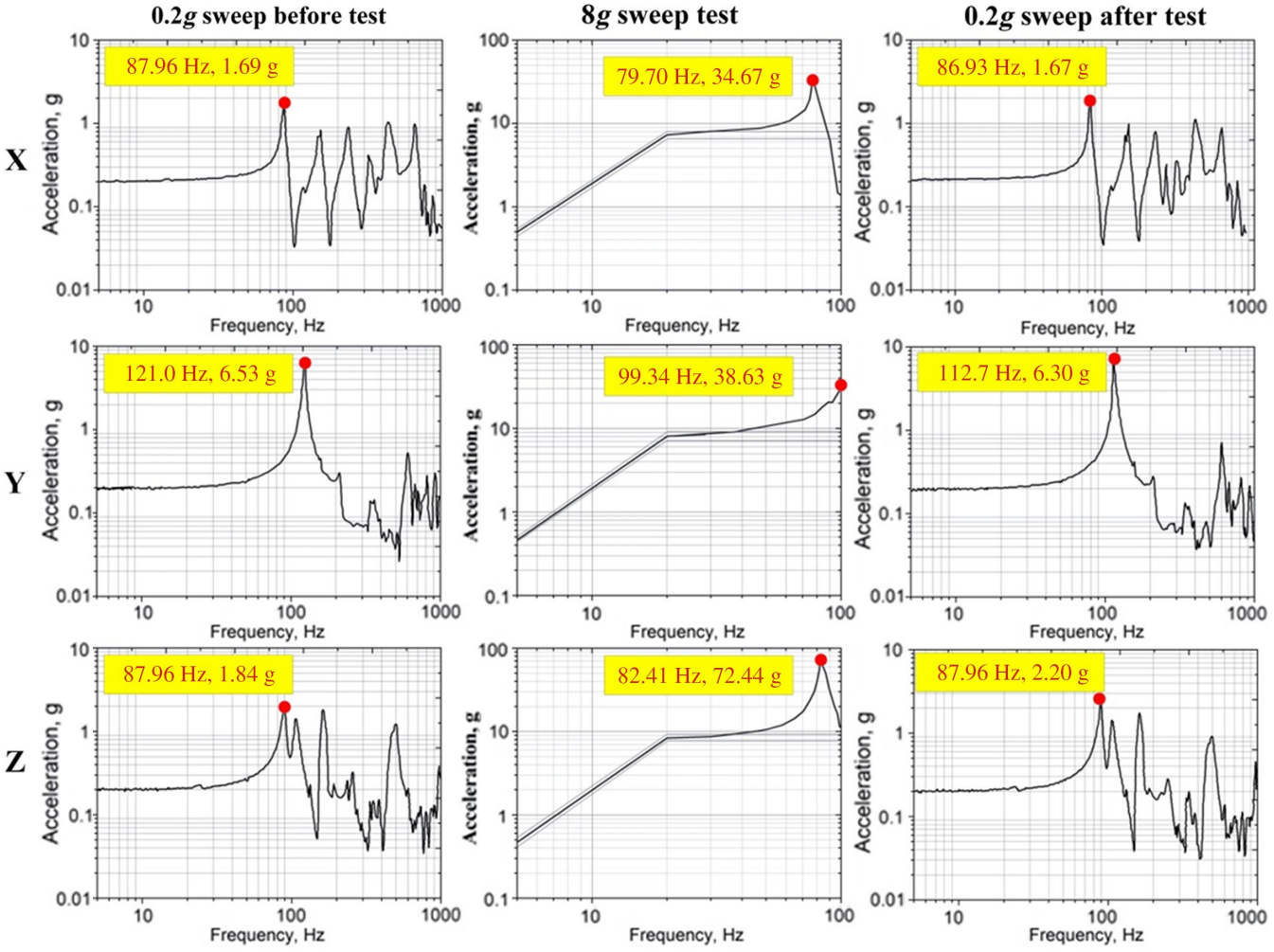

Fig. 11 Frequency response of the sine sweep of the smart solar array (folded state, point 1).

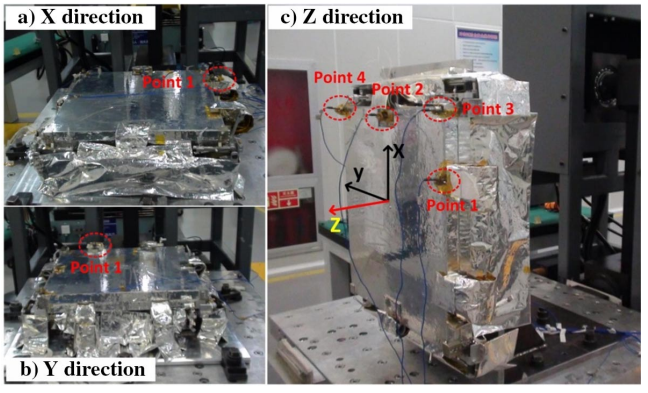

Fig. 12 Shocking test of the smart solar array.

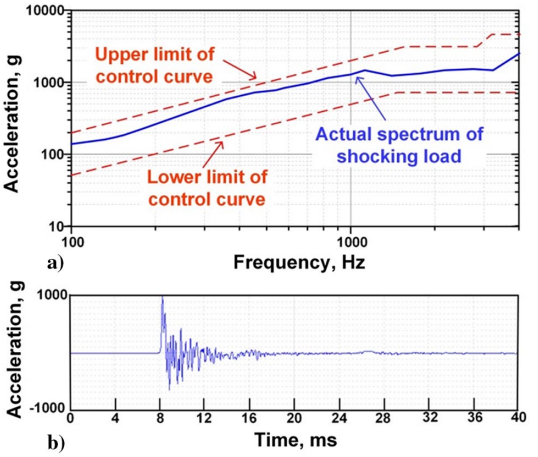

Fig. 13 Spectrum of shocking load (Fig. 13a) and the response result (Fig. 13b) of the smart solar array in the X direction.

3. *Acceleration Test (Folded State)*

An acceleration test is used to evaluate the static or quasi-static strength when the smart solar array is in the continuous acceleration conditions. The structural acceleration test was performed on a centrifuge 4 m in diameter with a test tolerance of 0–10% at an acceptance level, as displayed in Fig. 14. The length of the centrifuge arm was greater than five times the length of the test objects. The force direction of the component on the centrifuge was consistent with the actual force direction on the satellite during the launch stage; the loading rate was less than $5g$/ min. In addition, all electrical and electronic components (including all redundant circuits) during the test were energized as much as possible to monitor whether intermittent faults of the sensitive parameters occur during the launch stage. Components installed on the brackets were tested in all the three directions, namely, X, Y, and Z directions. For components requiring additional performance and functional testing, relevant tests were performed before and after the acceleration test, including electrical resistance of all the electrical heating chips and the microswitches. The acceptance level with an acceleration of $10g$ was applied along the three orthogonal axes of the satellite with the duration of at least 5 min. Video recording was performed during the acceleration test to observe if the structure was broken. After the

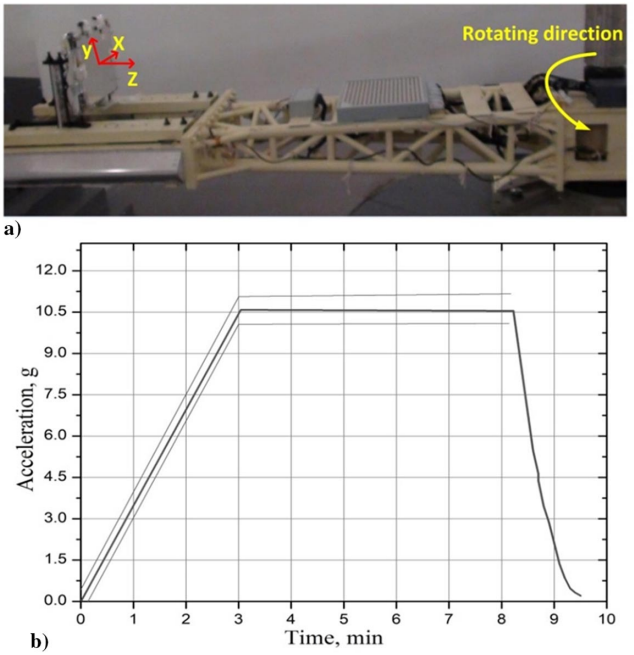

Fig. 14 Acceleration test (Fig. 14a) and the control curve (Fig. 14b) in the Z direction.

tests, the structure of the smart solar array was inspected, and all the components remained normal. Results indicated that the static or quasi-static strength of all the components of the smart solar array could satisfy the continuous acceleration conditions. Especially, it approved the safety of light components, including the heat insulation multilayer components covered on the SMPC locking mechanism as well as SMPC hinges, F46 film pasted on solar panel, wires, thermocouples, and microswitches.

4. *Noise Test (Folded State)*

Under the conditions of a wide frequency range and high-power noise during the launching process, the thin film components of the smart solar array may crack and break into pieces. Hence, the noise test should be conducted. During the noise experiment at the acceptance level, as presented in Fig. 15, the smart solar array was placed on the table at the center of the reverberation room at a 45 deg angle. No sponge was observed between the solar panel and the table. Four three-direction accelerometers were attached to solar panel 2. Figure 16 illustrates the sound pressure level at varied frequency ranges. The total sound pressure level did not exceed 143.5 dB, given the experimental standard. Video recording was also performed during the experiment to observe whether the structure was damaged, and the

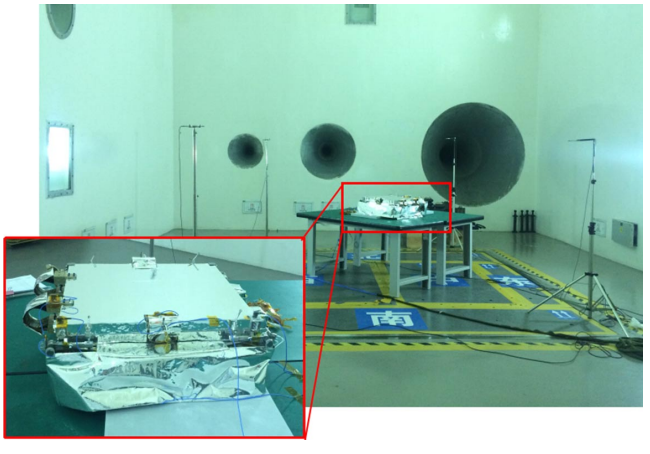

Fig. 15 Noise evaluation experiment of the smart solar array.

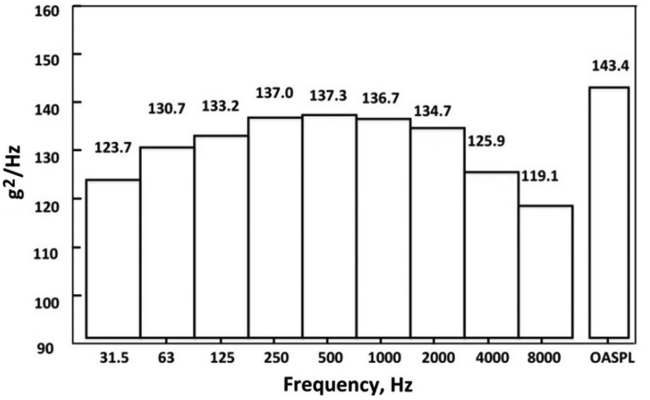

Fig. 16 Sound pressure levels at varied frequency range for noise evaluation experiment of the smart solar array.

electrical resistance of the electrical heating chip was measured. The structure was inspected after each experiment.

The start time of the noise evaluation experiment was 0 dB, and the test level was 142 dB with the experiment duration of 60 s. In Fig. 17, the comparison between the frequency responses of 0 and 40 s confirmed that the noise responses of the measuring point are consistent at this time. After the noisy evaluation, damage was not found on the film components, including electrical heating chips; the heat insulation multilayer components covered on the SMPC locking mechanism as well as SMPC hinges; and F46 film pasted on the solar panel, wires, thermocouples, and microswitches. Therefore, it revealed that the thin films would be safe under the conditions of a wide frequency range and high-power noise during launching process.

5. *Vibration Mode Test (Deployed State)*

The vibration mode of the smart solar array in a deployed state is important for the on-orbit attitude control of satellite, and it needs to test. In Fig. 18, an acceleration sensor was attached to each corner of every solar panel for data acquisition, transfer function, and modal analysis. A hammer with a rubber hammerhead was used to excite the full structure to obtain the frequency response characteristics. The envelope size of the flexible solar array after deployment was $381 \times 632 \times 1379$ mm, wherein the Z direction was perpendicular to the mounting surface. As the vibration response at the cores of the solar panel would be more sensitive than those located in the middle, eight unidirectional accelerometers were placed at the cores of two solar panels to measure the frequency response and vibration modes. The testing results indicated that the first natural frequency of the flexible solar array in the deployed state was 1.367 Hz, and the second frequency was 5.664 Hz. Based on design experiences, the minimum value of the fundamental frequency of deployed structures in space should be higher than 0.5 Hz, and therefore the fundamental frequency of the smart solar array (1.367 Hz) satisfies the demands of structure dynamics.

6. *Sinusoidal Sweep Vibration Test (Deployed State)*

To evaluate the vibration response of the smart solar array in the deployed state, a sinusoidal sweep experiment was performed to test whether the structure was damaged under the working condition, as exhibited in Fig. 19. Two flexible wires were used to hang the deployed solar array to offset gravity. The sinusoidal excitation force of the vibrator was applied on the metallic base of the solar array along the Y direction. The frequency sweep range was 5–500 Hz with a constant acceleration of $0.2g$. Because the vibration responses at the cores of the solar panel would be more sensitive than those located in the middle, four unidirectional accelerometers were selected to measure the resonance responses. The locations of point 1–point 4 in Fig. 19 were the same as those in Fig. 18. Therefore, as shown in Fig. 19, the four accelerometers are located at the backside of the solar panel, as highlighted by the labels of point 1–point 4. Measuring

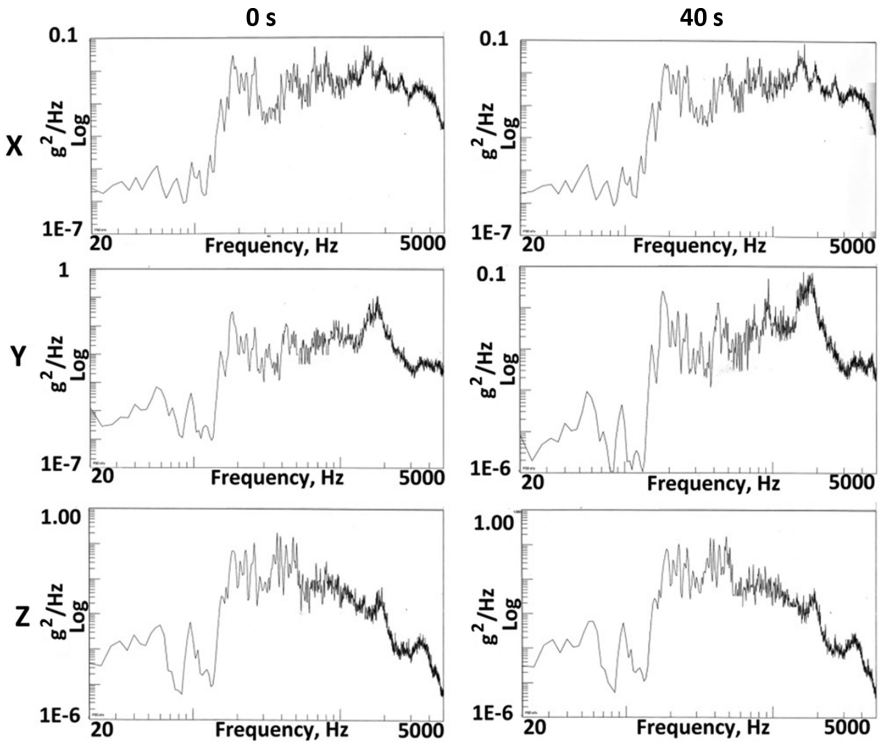

Fig. 17 Acceleration responses at 0 and 40 s at a typical point of the noise evaluation experiment of the smart solar array at X, Y, and Z directions.

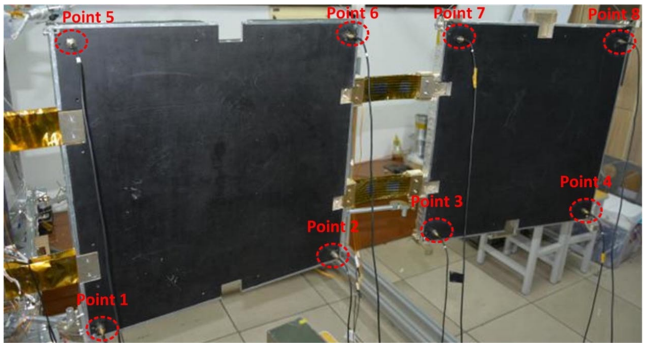

Fig. 18 Vibration mode test of the smart solar array in the deployed state.

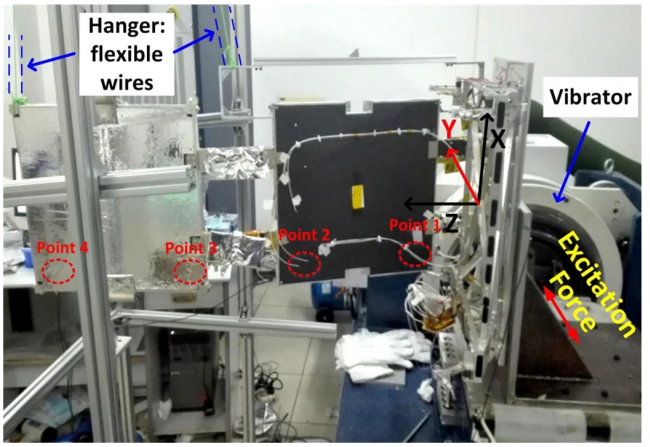

Fig. 19 Sine sweep vibration test of the smart solar array (the four measuring points are located at the backside of the solar panel as highlighted labels of point 1–point 4).

points 1–4 obtained the maximum peak-to-peak response values of 1.35, 2.68, 1.54, and 2.83g, correspondingly.

7. Flexibility Test (Deployed State)

Due to the orbital transfer of satellite, the shocking may apply on the deployed smart solar array, and therefore its deflection and strength need to be evaluated under possible shocking. In addition, if the deflection of the deployed smart solar array exceeds 100 cm, it will affect the working of the other adjacent experimental products aboard on the east deck of the satellite. In accordance with the design of the orbit dynamics of the satellite, the shock limit on the geostationary orbit could be equivalent to the 0.2g quasi-static loading applied to the smart solar array. The balloon suspension method was adopted to test the flexibility of the smart solar array in the deployed state. The base of the smart solar array was fixed, and the weight of each solar panel was unloaded through a rope connected to helium-filled balloons. The balance weight was suspended on the balloon to position the solar panel as desired. In this quasi-static flexibility test, 0.2g extra weight was statically added to the balloon on the basis of the balanced state. The results indicated that the maximum deflection of the solar array panel is at the tip point, and the deflection of the panel is less than 5.2 cm (at a distance of 20 cm from the fixed end).

In addition, the 0.2g quasi-static test was extended to a series of transient shockings (namely, 0.07, 0.1, and 0.2g) to understand the flexibility characteristics of the smart solar array in the deployed state under increasingly serious conditions. In this flexibility test of transient shocking, certain extra weight was transiently added to the balloon on the basis of the balanced state. Specifically, when the counterweight was instantaneously released, the video recorded the dynamical deflection of the two solar panels. Under the transient shockings of 0.07, 0.1, and 0.2g, the maximum amplitudes at the tip of the solar array were 31, 33, and 68 cm, respectively; the maximum amplitudes at a distance of 20 cm from the fixed end of the solar array were 5.1, 5.5, and 11.2 cm. The solar panel showed a higher oscillation amplitude in the transient shocking than in the quasi-static test.

After the quasi-static and transient shocking tests, the appearance and function of all the components were carefully checked, and no

damage was found in the structure. All the deflection amplitudes in the quasi-static and transient shocking tests satisfied the design of the stiffness and strength demands. The maximum deflection (68 cm, under the transient shocking of $0.2g$) was smaller than the deflection limit (100 cm), and therefore it would not affect the working of the other adjacent experimental products aboard on the east deck of the satellite.

B. Thermal Design and Vacuum Performance Verification

The satellite that carries the smart solar array was designed to be located on the geostationary orbit. The orbital height was 36,000 km, and the orbital period was greater than two years. The long-term sunshine mode was extensive on the geostationary orbit. The SMA and SMPC releasing mechanisms and the SMPC deployment mechanism had small heat capacities and were significantly affected by the space environment. The releasing and deployment mechanisms were mainly composed of SMA or SMPC materials, which were thermosensitive materials. The transition temperatures of the SMA and the SMPC of the releasing mechanisms were 95 and 210°C, correspondingly. The transition temperature of the SMPC deployment mechanisms was 150°C. Therefore, considering the safety margin, the main thermal control requirement was that the temperature of all components on the orbit is between −120 and +50°C.

In accordance with the aforementioned requirements, a thermal design scheme of the corresponding passive thermal control measures (namely, heat insulation multilayer components) was used. The thermal design of the smart solar array covered the thermal scheme and the corresponding simulation analysis, the installation of heat insulation components, the thermal balance experiment, and the evaluation of thermal vacuum cycling. Considering its complexity, another paper will detail the thermal design of the smart solar array in the near future. The present study only briefly introduces the thermal design and experimental validation of the smart solar arrays. In accordance with the external heat flow analysis results and the trajectory and structural characteristics, the following thermal control measures were determined, as displayed in Fig. 20:

1) The solar panel is covered with five units of heat insulation multilayer components, and the outermost layer of the multilayer insulation components is a single-sided aluminum-plated antistatic F46 film.

2) The solar panel +X direction has a heat-dissipating surface, which was pasted with F46 film with an area of 0.25 m^2.

3) Ten-millimeter polyimide heat insulation pads are installed between the base of the smart solar array and the satellite deck.

To verify the thermal design scheme of the smart solar array, acceptance-level thermal vacuum testing was conducted in a thermal vacuum tank. The temperature control point was located inside the heat insulation multilayer of the 90 deg hinge. The temperature measurements had 35 points. The testing conditions and environmental requirements were listed as follows: vacuum degree $\leq 6.65 \times 10^{-3}$ Pa; low temperature and tolerance of −95°C (−4–0°C); high temperature and tolerance of 60°C (0– + 4°C); number of thermal cycles of 3.5 times; temperature change rate: average temperature change rate $\geq 1°C/\text{min}$; and thermal balance: temperature fluctuation is smaller than 0.5°C in 4 h. In Fig. 21, the thermal balance results indicated that the temperatures of the key points satisfied the design specifications.

C. SMA Releasing Mechanism

The SMA tube is the main component of the SMA releasing mechanism. The material of the SMA is Ti-6Al-4V (TC4). The resistance of an SMA rod is 7.8 Ω with an actuation voltage of 12 V and a power of 18 W. When heated above the transition temper-

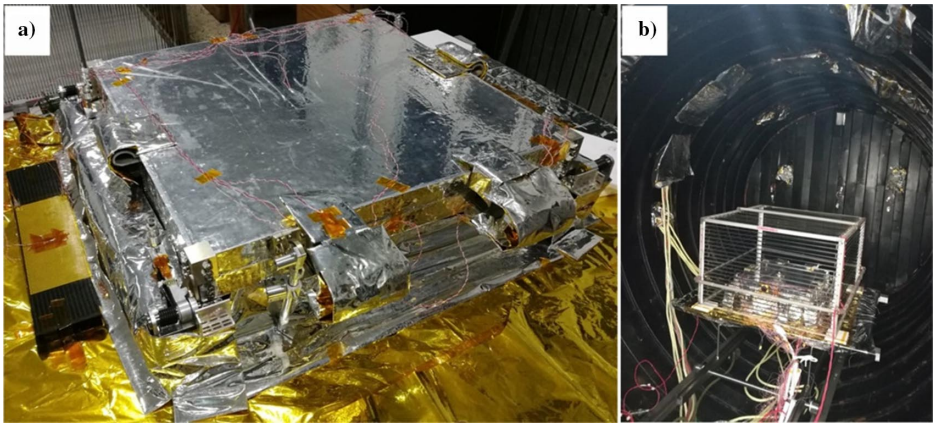

Fig. 20 Flexible heat insulation multilayer components (Fig. 20a) and the thermal vacuum test (Fig. 20b) of the smart solar array.

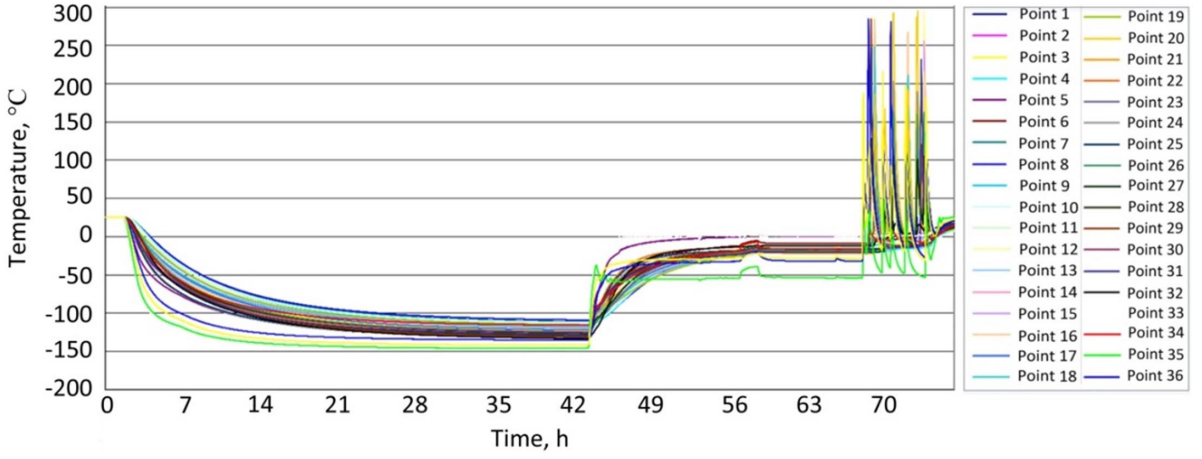

Fig. 21 Temperature history of the thermal balance of the smart solar array.

Table 3 Unlocking performance of the SMA releasing mechanism at varying ambient temperatures

Temperature, °C	Voltage, V	Current, A	Releasing time, s
60	9	1.15	25
25	11	1.41	38
−50	16	2.05	39

ature (95°C) of the SMA tube, the length of the SMA tube increased, and its maximum force exceeded 10,000 N. When the SMA tube was electrically heated, the length of the SMA tube was increased to apply a braking force to the slotted bolt in the axial direction, and the slotted bolt was broken at its weak portion. After fracturing the slotted bolt, both parts of the bolt had a certain amount of kinetic energy, and the broken bolts are buffered and stored by the capturing cap. The calibration results indicated that a locking force of 2000 N can be reliably applied to the bolt by applying a torque of 6.67 N/m to the titanium nut using a torque wrench. To evaluate the releasing performance at varying ambient temperatures comprehensively, the releasing tests were conducted using the results summarized in Table 3. The unlocking time of the SMA releasing mechanism could be completed within 40 s.

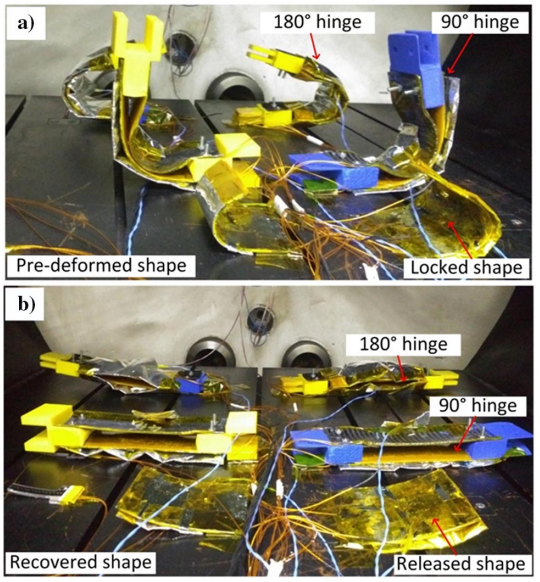

Fig. 22 Recovery performance of the SMPC releasing mechanism and SMPC hinges in a vacuum environment (12×10^{-3} Pa, 25°C).

D. SMPC Releasing Mechanism and SMPC Deployment Hinge

For the SMPC releasing mechanism, the locking performance was characterized by testing the recovery angle of the locking SMPC laminate after a certain period of time in a certain environment. The SMPC locking laminate has a bending radius of 8 mm and a bending angle of 145 deg. The releasing mechanism was maintained at an ambient temperature of 85°C (35°C higher than the highest temperature in the thermal design; that is, 50°C) for 240 h. The results indicate that the fixing rate of the SMPC locking laminate is 100%. Regarding the viscoelastic effect, the cyclic loading and unloading experiments of the SMPC have been conducted at a temperature of 120°C [15]. The stress–strain curves show an obvious hysteresis, reflecting the energy dissipation and the stress relaxation during each cycle. The results also demonstrate that the SMPC holds the ability to repeatedly deform and recover without losing the shape-memory effect.

The recovery performance of the SMPC releasing mechanism and SMPC hinges was tested under a vacuum environment (1×10^{-3} Pa, 25°C), as exhibited in Fig. 22. The shape recovery duration of the single SMPC hinge was approximately 110–120 s with a shape recovery ratio of 98–100% under an actuation power of 50 W (250 Ω) for each hinge. The maximum shape recovery torsion was 0.15–0.20 N/m. The shape recovery duration of the SMPC releasing mechanism was approximately 240–270 s with a shape recovery ratio of 90–95% at the actuation power of 29 W (250 Ω).

E. Deployment Evaluation of the Smart Solar Array

In Fig. 23a, the balloon suspension method was designed to overcome the gravity on the ground to simulate the space microgravity environment. Solar panel 1 was suspended through four strings connected to the ring balloon. Solar panel 2 was also suspended through one string connected to the ring balloon. To adjust the balance, the balance weight was placed in a small bag hanging on each string. The 90 deg SMPC hinge connected the base with solar panel 1; and the 90 deg SMPC hinge connected solar panel 1 with solar panel 2.

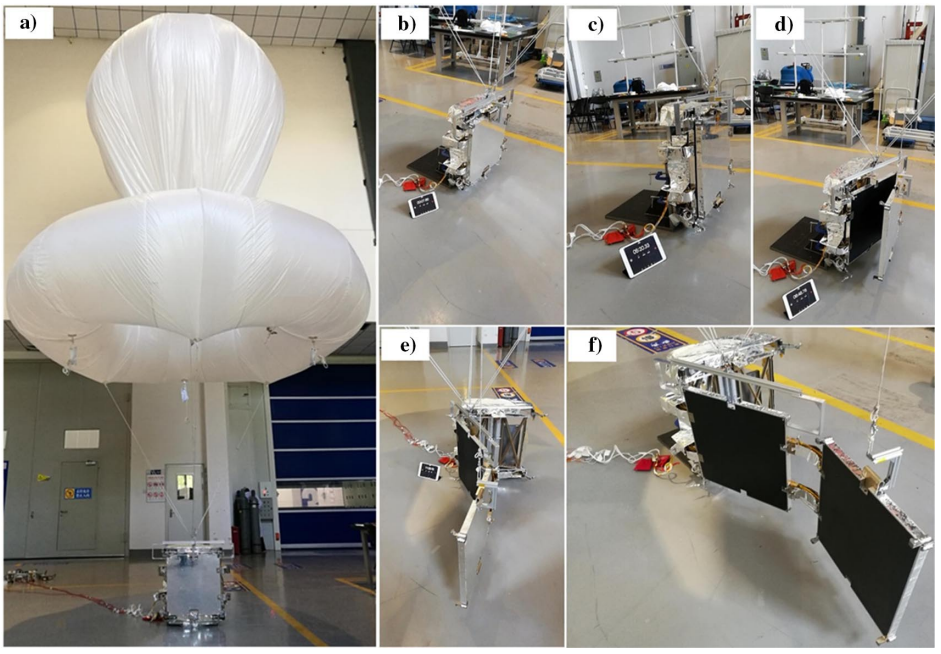

Fig. 23 Unlocking and deployment process of the smart solar array.

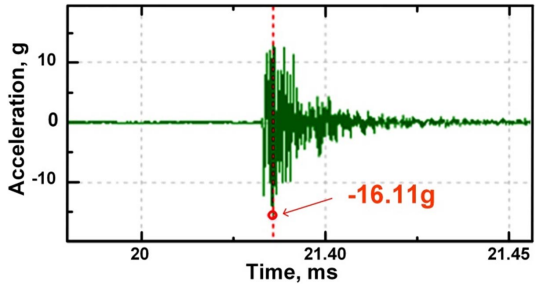

Fig. 24 Time-domain shocking response during the releasing process of the SMA releasing mechanism.

In Figs. 23b–23f, the entire working procedure was recorded in a 23 deg atmospheric environment as follows:

1) The electrical heating circuit and balloon suspension systems were inspected before deployment. Heating circuit 1 was energized at 18.36 W (7.8 Ω). The unlocking operation of the SMA releasing mechanism was completed within 32 s, which was indicated by the changes in the microswitch output electric potential. Then, heating circuit 1 was powered off. In Fig. 24, the maximum acceleration of the shocking of the SMA releasing mechanism was tested at 13–16g in 0.005–0.01 s, and the attenuation cutoff time was 0.03 s.

2) Heating circuit 2 was energized, and the SMPC releasing mechanism was unlocked within 252 s. Meanwhile, heating circuit 2 was powered off.

3) Heating circuits 3 and 4 were energized, and the two 90 deg SMPC hinges were heated and deployed to the designed position within 175 s, where the dowel of the 90 deg locking mechanism was automatically inset into its pinhole and locked deployed solar panel 1. Afterward, heating circuits 3 and 4 were powered off.

4) Subsequently, heating circuits 5 and 6 were energized, and the two 180 deg SMPC hinges were heated and deployed to the designed position within 161 s, where the 180 deg locking mechanism locked deployed solar panel 2. Finally, heating circuits 5 and 6 were also powered off.

This smart solar array was installed on the east desk of the SJ-18 satellite (Earth synchronous orbit; 36,000 km), which was launched by the Long-March-5 Heavy Rocket on 2 July 2017 at the Wenchang Satellite Launching Center of China. The smart solar array successfully withstood the harsh mechanics environment of the first 900 s during the launching process, which preliminary verified the overall performance of the mechanical design and locking. Unfortunately, due to the abnormal state of the rocket, the satellite failed to launch into the designed orbit, and the releasing and deployment performance of this smart solar array was not verified on orbit.

IV. Discussions and Future Prospections

In this study, the smart solar array was locked by SMA- and SMPC-based devices and deployed by SMPC-based actuation hinges. No traditional electroexplosive devices or mechanical hinge driving mechanisms were used in this smart solar array. Thus, this study is a prospective exploration and innovation for the next general space locking/releasing mechanisms and superlarge space deployable structures. All designs, simulations, manufacturing, and experiments strictly followed China's aerospace standard. After final acceptance evaluation, the smart solar array was delivered to the China Academy of Space Technology. Note that this study mainly aimed to investigate the applications of SMAs and SMPCs in solar arrays. Therefore, the solar panels were just solar panel substrates, which do not contain photovoltaic cells.

In summary, the SMA and SMPC releasing mechanisms are suitable for locking forces below 2000 and 200 N, respectively; their locking stiffness and deformation ability are stable in eight shape recovery cycles. The SMPC hinge demonstrates a recovery torsion of 0.1–0.2 N/m and a shape recovery duration of approximately 3 min; the shape recovery performance is relatively stable at 10 deformation cycles. However, in comparison with traditional electroexplosive devices or mechanical hinge driving mechanisms, SMA- and SMPC-based releasing or deployable mechanisms still expose some weaknesses. For the SMA and SMPC releasing mechanisms, the unlocking time cannot be controlled in a narrow period (SMA releasing mechanism: 25–40 s; and SMPC releasing mechanism: 240–270 s) due to material instability or atmosphere temperature. SMAs and SMPCs are thermosensitive materials; therefore, the atmosphere temperature of their applications in releasing or deployment devices must be strictly limited and controlled to at least 15–30°C lower than the transition temperature of the shape-memory materials. The locking stiffness of the SMPC materials remains low, thereby suggesting that these materials can be individually used for locking the structures with a small mass (e.g., smaller than 0.5 kg).

This study only provides the general concepts, designs, and experimental evaluation results of the smart solar array. In the future, three other studies will discuss the following contexts in detail: 1) structural finite element analysis and optimization of the smart solar array; 2) thermal simulation, design, and experimental verification of the smart solar arrays; and 3) design and experimental verification of SMPC releasing mechanisms.

V. Conclusions

In accordance with China's aerospace standards and on the basis of shape-memory materials, the design and performance evaluations of the smart solar array were conducted to achieve high stiffness locking, low impact unlocking, and slow controllable deployment. The smart solar array was locked by one SMA- and two SMP-based releasing mechanisms and deployed using four SMPC-based hinges. To evaluate the smart solar array systematically, various performance tests were conducted, including structural dynamics in a folded state (sinusoidal sweep vibration, shocking, acceleration, and noise) and a deployed state (mode, sinusoidal sweep, and flexibility), thermal design, locking and releasing, deployment, and self-locking after deployment. The results indicated that the experimental performance satisfies the design requirements of the smart solar array. Moreover, the SMA and SMPC releasing mechanisms are suitable for locking forces below 2000 and 200 N, correspondingly; the locking stiffness and deformation ability are stable in eight shape recovery cycles for both models. The SMPC hinge performs a recovery torsion of 0.1–0.2 N/m and a shape recovery duration of approximately 3 min; the shape recovery performance is relatively stable in 10 deformation cycles. As shape-memory materials, SMAs and SMPCs possess characteristics of low shocking and repeated usage, thereby making them suitable for locking separable structures with a small mass. The SMPCs show a macroscale compressive strain of 8–10% in the soft state and the same magnitude level of stiffness as the traditional fiber-reinforced composite in the hard state. Thus, they are suitable for use in next-generation superlarge space deployment structures.

Acknowledgments

This work is supported by the National Natural Science Foundation of China (grant no. 11632005). Xin Lan and Liwu Liu contributed equally to this work.

References

[1] Liu, Y. J., Du, H. Y., Liu, Y. J., and Leng, J. S., "Shape Memory Polymers and Their Composites in Aerospace Applications: A Review," *Smart Materials and Structures* Vol. 23, No. 2, 2014, Paper 023001. https://doi.org/10.1088/0964-1726/23/2/023001

[2] Fang, H. B., Li, S. Y., Ji, H. M., and Wang, K. W., "Dynamics of a Bistable Miura-Origami Structure," *Physical Review E*, Vol. 95, No. 5, 2017, Paper 052211. https://doi.org/10.1103/PhysRevE.95.052211

[3] Blumenschein, L. H., Gan, L. T., and Fan, J. A., "A Tip-Extending Soft Robot Enables Reconfigurable and Deployable Antennas," *IEEE Robotics and Automation Letters*, Vol. 3, No. 2, 2018, pp. 949–956. https://doi.org/10.1109/LRA.2018.2793303

[4] Bakis, C. E., Bank, L. C., Brown, V. L., Cosenza, E., Davalos, J. F., Lesko, J. J., Machida, A., Rizkalla, S. H., and Triantafillou, T. C., "Fiber-Reinforced Polymer Composites for Construction-State-of-the-Art

Review," *Journal of Composites for Construction*, Vol. 6, No. 2, May 2002, pp. 73–87.
https://doi.org/10.1061/(ASCE)1090-0268(2002)6:2(73)

[5] Murphey, T. W., Francis, W., Davis, B., and Mejia-Ariza, J. M., "High Strain Composites," *2nd AIAA Spacecraft Structures Conference, AIAA SciTech*, AIAA Paper 2015-0942, 2015.

[6] Christian, M., Chilan, D. R., Herber, Y. N., Soon-Jo, C., James, T. A., Jack, B. A., and Oscar, S. A., "Co-Design of Strain-Actuated Solar Arrays for Spacecraft Precision Pointing and Jitter Reduction," *AIAA Journal*, Vol. 55, No. 9, 2017, pp. 3180–3195.
https://doi.org/10.2514/1.J055748

[7] Sharma, A., Rose, T., Seamone, A., and Jiménez, F. L., "Analysis of the Column Bending Test for Large Curvature Bending of High Strain Composites," *AIAA SciTech 2019 Forum*, AIAA Paper 2019-1746, 2019, pp. 1–15.
https://doi.org/doi:10.2514/6.2019-1746

[8] Ko, K. E., and Kim, J. H., "Thermally Induced Vibrations of Spinning Thin-Walled Composite Beam," *AIAA Journal*, Vol. 41, No. 2, 2003, pp. 296–303.
https://doi.org/10.2514/2.1943

[9] Michael, A. E., Mark, J. S., Evelyn, D. E., and Michael, P., "Recent Developments in Precision High Strain Composite Hinges for Deployable Space Telescopes," *AIAA Spacecraft Structures Conference, AIAA SciTech Forum*, AIAA Paper 2018-0939, 2018, pp. 1–0.
https://doi.org/10.2514/6.2018-0939

[10] Sungeun, K. J., Jeremy, A., and Banik, M. P., "Free Deployment of a Sparse-Isogrid Column with High Strain Composite Ribs," *3rd AIAA Spacecraft Structures Conference, AIAA SciTech Forum*, AIAA Paper 2016-0971, 2016, pp. 1–12.
https://doi.org/10.2514/6.2016-0971

[11] Lin, K. H., Carl, F. K., and Cliff, E. W., "Shape Memory Rigidizable Inflatable (RI) Structures for Large Space Systems Applications," *47th AIAA/ASME/ASCE/AHS/ASC Structures, Structural Dynamics, and Materials Conference*, AIAA Paper 2006-1896, 2006, pp. 1–10.
https://doi.org/10.2514/6.2006-1896

[12] Hoang, B., Spence, B., White, S., and Kiefer, S., "Commercialization of Deployable Space Systems Roll-Out Solar Array (ROSA) Technology for Space Systems Loral (SSL) Solar Arrays," *2016 IEEE Aerospace Conference*, IEEE Publ., Piscataway, NJ, 2016.
https://doi.org/10.1109/AERO.2016.7500723

[13] Banik, J., Chapman, D., and Merrill, J., "International Space Station (ISS) Roll-Out Solar Array (ROSA) Spaceflight Experiment Mission and Results," *IEEE 7th World Conference on Photovoltaic Energy Conversion (WCPEC) (A Joint Conference of 45th IEEE PVSC, 28th PVSEC and 34th EU PVSEC)*, Inst. of Electrical and Electronics Engineers, New York, 2018.
https://doi.org/10.1109/PVSC.2018.8548030

[14] Leng, J. S., Lan, X., Liu, Y. J., and Du, S. Y., "Shape Memory Polymers and Their Composites: Stimulus Methods and Applications," *Progress in Materials Science*, Vol. 56, No. 7, 2011, pp. 1077–1135.
https://doi.org/10.1016/j.pmatsci.2011.03.001

[15] Li, F. F., Scarpa, F., Lan, X., Liu, L. W., Liu, Y. J., and Leng, J. S., "Bending Shape Recovery of Unidirectional Carbon Fiber Reinforced Epoxy-Based Shape Memory Polymer Composites," *Composites, Part A: Applied Science and Manufacturing*, Vol. 116, Jan. 2019, pp. 169–179.
https://doi.org/10.1016/j.compositesa.2018.10.037

[16] Barrett, R., Francis, W., Abrahamson, E., Lake, M., and Scherbarth, M., "Qualification of Elastic Memory Composite Hinges for Spaceflight Applications,"*47th AIAA/ASME/ASCE/AHS/ASC Structures, Structural Dynamics, and Materials Conference 14th AIAA/ASME/AHS Adaptive Structures 7th Conference*, AIAA Paper 2006-2039, 2006.
https://doi.org/10.2514/6.2006-2039

[17] Dietsch, B., and Tong, T., "A Review—Features and Benefits of Shape Memory Polymers (SMPs)," *Journal of Advanced Materials*, Vol. 39, No. 2, 2007, pp. 3–12.

[18] Koerner, H., Strong, R. J., Smith, M. L., Wang, D. H., Tan, L. S., Lee, K. M., White, T. J., and Vaia, R. A., "Polymer Design for High Temperature Shape Memory: Low Crosslink Density Polyimides," *Polymer*, Vol. 54, No. 1, 2013, pp. 391–402.
https://doi.org/10.1016/j.polymer.2012.11.007

[19] Lan, X., Liu, L. W., Liu, Y. J., Leng, J. S., and Du, S. Y., "Post Microbuckling Mechanics of Fibre-Reinforced Shape-Memory Polymers Undergoing Flexure Deformation," *Mechanics of Materials*, Vol. 72, May 2014, pp. 46–60.
https://doi.org/10.1016/j.mechmat.2013.05.012

[20] Wang, Z. D., Li, Z. F., Xiong, Z. Y., and Wang, L.Y., "Theoretical Studies on Microbuckling Mode of Elastic Memory Composites," *Acta Mechanica Solida Sinica*, Vol. 23, No. 1, 2010, pp. 20–28.
https://doi.org/10.1016/S0894-9166(10)60003-1

[21] Zhang, J. M., Dui, G. S., and Liang, X. Y., "Revisiting the Micro-Buckling of Carbon Fibers in Elastic Memory Composite Plates Under Pure Bending," *International Journal of Mechanical Sciences*, Vol. 136, Feb. 2018, pp. 339–348.
https://doi.org/10.1016/j.ijmecsci.2017.12.018

[22] Lan, X., Liu, L. W., Liu, Y. J., and Leng, J. S., "Macroscale Bending Large-Deformation and Microbuckling Behavior of a Unidirectional Fiber Reinforced Soft Composite," *Journal of Composite Materials*, Vol. 54, No. 2, 2020, pp. 243–257.
https://doi.org/10.1177/0021998319854145

[23] Barrett, R., Francis, W., Abrahamson, E., and Lake, M. S., "Qualification of Elastic Memory Composite Hinges for Spaceflight Applications," *47th AIAA/ASME/ASCE/AHS/ASC Structures, Structural Dynamics, and Materials Conference*, AIAA Paper 2006-2039, 2006, pp. 1–10.
https://doi.org/10.2514/6.2006-2039

[24] Liu, Z. X., Li, Q. F., Bian, W. F., Lan, X., Liu, Y. J., and Leng, J. S., "Preliminary Test and Analysis of an Ultralight Lenticular Tube Based on Shape Memory Polymer Composites," *Composite Structures*, Vol. 223, Sept. 2019, Paper 110936.
https://doi.org/10.1016/j.compstruct.2019.110936

[25] Lagrange, R., Jiménez, F. L., Terwagne, D., Brojan, M., and Reis, P. M., "From Wrinkling to Global Buckling of a Ring on a Curved Substrate," *Journal of the Mechanics and Physics of Solids*, Vol. 89, April 2016, pp. 77–95.
https://doi.org/10.1016/j.jmps.2016.02.004

[26] Rahman, A. A., Ikeda, T., and Senba, A., "Memory Effects Performance of Polyurethane Shape Memory Polymer Composites (SMPC) in the Variation of Fiber Volume Fractions," *Fiber Polymer*, Vol. 18, No. 5, 2017, pp. 979–986.
https://doi.org/10.1007/s12221-017-6687-9

[27] Takeda, T., Narita, F., and Shindo, Y., "Failure of Hybrid Beams Consisting of Woven Carbon Fiber Composite and Shape Memory Polymer Layers Under Flexural Loading," *Journal of Sandwich Structures and Materials*, Vol. 18, No. 1, 2016, pp. 113–128.
https://doi.org/10.1177/1099636215607395

[28] Santo, L., Quadrini, F., Squeo, E. A., Dolce, F., Mascetti, G., Bertolotto, D., Villadei, W., Ganga, P. L., and Zolesi, V., "Behavior of Shape Memory Epoxy Foams in Microgravity: Experimental Results of STS-134 Mission," *Microgravity Science and Technology*, Vol. 24, No. 4, 2012, pp. 287–296.
https://doi.org/10.1007/s12217-012-9313-x

[29] Santo, L., Quadrini, F., Ganga, P. L., and Zolesi, V., "Mission BION-M1: Results of Ribes/Foam2 Experiment on Shape Memory Polymer Foams and Composites," *Aerospace Science and Technology*, Vol. 40, April 2015, pp. 109–114.
https://doi.org/10.1016/j.ast.2014.11.008

[30] Li, F. F., Liu, L. W., Lan, X., Pan, C. T., Liu, Y. J., Leng, J. S., and Xie, Q., "Ground and Geostationary Orbital Qualification of a Sunlight-Stimulated Substrate Based on Shape Memory Polymer Composite," *Smart Materials and Structures*, Vol. 28, No. 7, 2019, Paper 075023.
https://doi.org/10.1088/1361-665X/ab18b7

[31] Zhao, L. H., Wang, H., Chen, G. L., and Huang, S. Z., "Sequentially Assembled Reconfigurable Extended Joints: Self-Lockable Deployable Structure," *Journal of Aerospace Engineering*, Vol. 31, No. 6, 2018, Paper 04018103.
https://doi.org/10.1061/(ASCE)AS.1943-5525.0000877

[32] Otsuka, K., and Makihara, K., "Deployment Simulation Using Absolute Nodal Coordinate Plate Element for Next-Generation Aerospace Structures," *AIAA Journal*, Vol. 56, No. 3, 2018, pp. 1266–1276.
https://doi.org/10.2514/1.J056477

[33] Zhang, D. D., Zhao, Q. L., Li, F., Tao, J., and Gao, Y. F., "Torsional Behavior of a Hybrid FRP-Aluminum Space Truss Bridge: Experimental and Numerical Study," *Engineering Structures*, Vol. 157, Feb. 2018, pp. 132–143.
https://doi.org/10.1016/j.engstruct.2017.12.013

[34] Maji, A., Mahnke, S. M., and Thomas, W., "Actuation of Neutrally Stable Composite Tape-Springs with Shape Memory Alloy," *Journal of Advanced Materials*, Vol. 41, No. 1, 2009, pp. 18–33.

[35] Jacobs, S., Coconnier, C., DiMaio, D., Scarpa, F., Toso, M., and Martinez, J., "Deployable Auxetic Shape Memory Alloy Cellular Antenna Demonstrator: Design, Manufacturing and Modal Testing," *Smart Materials and Structures*, Vol. 21, No. 7, 2012, Paper 075013.
https://doi.org/10.1088/0964-1726/21/7/075013

[36] Katsumata, N., Kume, M., and Higuchi, K., "Deployment Behavior Control Using Cables and Bi-Shape Memory Alloy Convex Tape Booms," *Advances in Mechanical Engineering*, Vol. 9, No. 7, 2017, pp. 1–8.
https://doi.org/10.1177/1687814017707909

[37] Jacobs, S., Coconnier, C., DiMaio, D., Scarpa, F., Toso, M., and Martinez, J., "Deployable Auxetic Shape Memory Alloy Cellular Antenna Demonstrator: Design, Manufacturing and Modal Testing," *Smart Materials and Structures*, Vol. 21, No. 7, 2012, Paper 075013. https://doi.org/10.1088/0964-1726/21/7/075013

[38] Xie, F., Huang, L. N., Liu, Y., and Leng, J., "Synthesis and Characterization of High Temperature Cyanate-Based Shape Memory Polymers with Functional Polybutadiene/Acrylonitrile," *Polymer*, Vol. 55, No. 23, 2014, pp. 5873–5879. https://doi.org/10.1016/j.polymer.2014.07.035

[39] Liu, T., Liu, L. W., Yu, M., Li, Q., Zeng, C., Lan, X., Liu, Y., and Leng, J., "Integrative Hinge Based on Shape Memory Polymer Composites: Material, Design, Properties and Application," *Composite Structures*, Vol. 206, Dec. 2018, pp. 164–176. https://doi.org/10.1016/j.compstruct.2018.08.041

[40] Liu, Z. X., Lan, X., Bian, W. F., Liu, L. W., Li, Q. F., Liu, Y. J., and Leng, J. S., "Design, Material Properties and Performances of a Smart Hinge Based on Shape Memory Polymer Composites," *Composites, Part B: Engineering*, Vol. 193, July 2020, Paper 108056. https://doi.org/10.1016/j.compositesb.2020.108056

C. Bisagni
Associate Editor